ON METHODS FOR CALIBRATING THE HEAT EXCHANGER OF A MODEL FOR SIMULATING THE THERMAL AND ELECTRICAL PRODUCTION OF SMALL-SCALE SOLID-OXIDE FUEL CELL COGENERATION SYSTEMS

Ian Beausoleil-Morrison[1], Kathleen Siemens[1], and Stephen Oikawa[2]

[1] CANMET Energy Technology Centre, Natural Resources Canada, Ottawa Canada
[2] Formerly with Fuel Cell Technologies Ltd., Kingston Canada

ABSTRACT

The methods used to empirically calibrate the model representing a heat exchanger that recovers thermal energy from a solid-oxide fuel cell cogeneration systems have been demonstrated. The design of the experiments that were conducted to derive calibration data for the model and the propagation of measurement uncertainty into the calibration data were treated. Regression methods were then employed to establish all inputs necessary to characterize the heat exchanger of a prototype 5 kW device.

1. INTRODUCTION

Residential cogeneration is an emerging technology with a high potential to deliver energy services with increased efficiency and environmental benefits. The concurrent production of electricity and heat from a single fuel source can reduce primary energy consumption and associated greenhouse gas emissions. The decentralized production of electricity also has the potential to reduce electrical transmission and distribution congestion and to alleviate utility peak demand problems. A number of manufacturers worldwide are developing residential-scale cogeneration devices based upon fuel cells, internal combustion engines, and Stirling cycles (Knight and Ugursal, 2005).

The effective exploitation of the cogeneration device's thermal output for space heating, space cooling, and/or heating domestic hot water is crucial to realizing high levels of overall energy efficiency and the associated environmental benefits. Consequently, the performance of these devices will be highly dependent upon how the cogeneration device is integrated to service the host building's thermal and electrical demands. In order to accurately assess performance, therefore, it is imperative that models of cogeneration devices be incorporated into whole-building simulation tools that account for the interactions between the building and its environment, the occupants, the thermal and electrical production and distribution systems, and energy management and control systems.

These factors motivated the formation of Annex 42 of the International Energy Agency's Energy Conservation in Buildings and Community Systems Programme (IEA/ECBCS). This international collaborative project aims to develop, validate, and implement models of cogeneration devices for whole-building simulation programs. The mathematical model that IEA/ECBCS Annex 42 has developed for simulating the performance of solid oxide fuel cell (SOFC) cogeneration devices is described by Beausoleil-Morrison *et al.*

(2006). This is a system-level model that considers the thermodynamic performance of all components that consume energy and produce the SOFC-cogeneration device's thermal and electrical output. The model relies heavily upon empirical information that can be acquired from the testing of coherent systems or components and is designed for operation at a time resolution that is in the order of minutes.

The current paper treats the calibration of the IEA/ECBCS Annex 42 SOFC-cogeneration model using empirical data gathered through experiments conducted on a prototype 5 kW SOFC-cogeneration system. Following a brief review of pertinent aspects of the model, the paper details the experimental protocol that was developed for the purposes of model calibration and empirical validation. The experimental equipment and measurement methods employed are then be described. The propagation of measurement uncertainty into derived quantities is treated and the methods utilized to calibrate model inputs based upon these data are then elaborated. Concluding remarks are then provided along with recommendations for future work. As space limitations do not permit the treatment of all aspects of the model, this paper demonstrates the calibration methodology by focusing upon the heat exchanger that produces the SOFC-cogeneration devices' thermal output.

2. DESCRIPTION OF SOFC-COGENERATION MODEL

2.1 Solid-Oxide Fuel Cell Cogeneration

Fuel cells are energy conversion devices that directly convert chemical energy to electrical energy. This is accomplished through the electrochemical oxidation of a fuel and the electrochemical reduction of oxygen. These electrochemical reactions occur at electrodes which are continuously fed with fuel and oxygen and which are separated by an electrolyte layer.

SOFCs use a solid metal oxide as the electrolyte. These show particular promise for residential cogeneration applications because of their ability to internally reform natural gas, and due to their high operating temperature (600 to 1 000^oC), they produce high quality thermal energy that can be exploited for space heating, space cooling, and/or DHW heating. The interested reader is referred to Singhal and Kendall (2003) for a thorough review of SOFC technology and to Ellis and Gunes (2002) for a discussion on the use of fuel cells for building cogeneration.

It is important to note that the fuel cell stack itself is only a single component within a complex energy conversion system. Figure 1 illustrates one possible system configuration of a SOFC-cogeneration device[1]. Besides the fuel cell stack (shown in grey), the system might include: an afterburner to combust unreacted fuel; an air filter and preheater; a fuel desulfurizer, pre-heater, pre-reformer, and reformer; and water preparation. A compressor may be required to supply pressurized fuel while a blower will likely be present to supply air to provide oxygen to support the electrochemical and combustion reactions. A pump may also be required to supply liquid water for steam reformation purposes. A battery could be used for buffering the fuel cell stack's DC electrical

[1] Some energy flows (e.g. thermal inputs to the desulfurizer and fuel pre-heater) are not illustrated in the figure for the sake of clarity. Also, intra-control-volume energy flows are not considered within the model.

production and for meeting load transients and the system will include a power conditioning unit to convert the electrical output to AC. All SOFC-cogeneration systems will include a heat recovery device that transfers the heat of the hot product gases to the building's HVAC system. Some systems may include an integrated auxiliary burner that is activated when the fuel cell cannot satisfy the building's thermal loads.

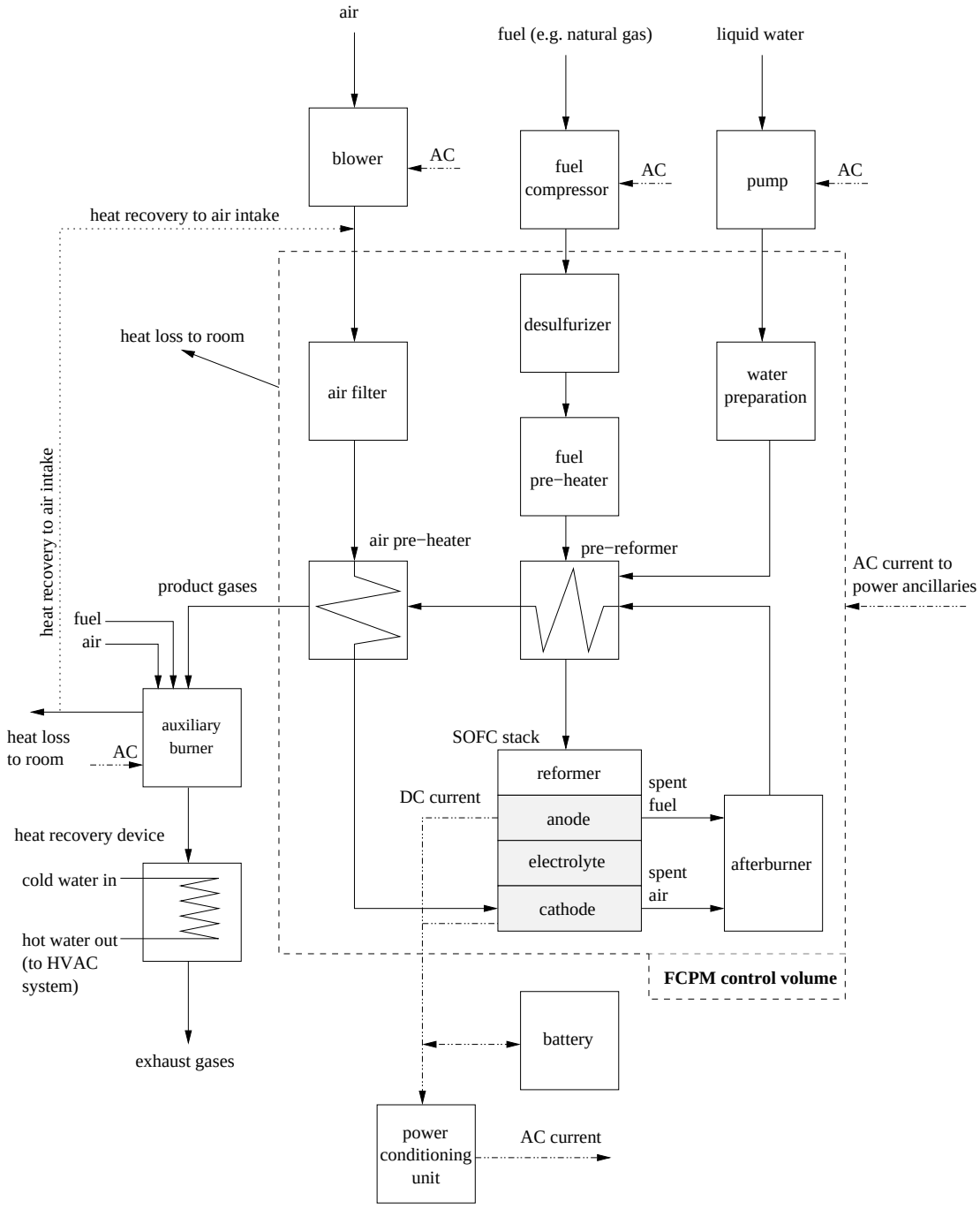

Figure 1: One possible system configuration of a SOFC-cogeneration device

2.2 Model Topology

Many detailed SOFC models are presented in the literature. However, most of these are not well suited for the purposes of evaluating the energy performance of SOFC-cogeneration devices since they focus on single cells or stacks of cells while other components (refer to Figure 1) are left untreated (e.g. Beale *et al.*, 2003; Bove *et al.*, 2005). Other researchers have applied models at the other end of the resolution spectrum to examine the performance of complete SOFC-cogeneration systems (Braun, 2002; Sicre *et al.*, 2005; Dorer *et al.*, 2005; Hawkes and Leach, 2005). However, in these contributions the SOFC-cogeneration device has been modelled using a performance map (derived either from empirical evidence or from detailed modelling performed outside the context of whole-building simulation) that decouples the electrical and thermal performance of the cogeneration device from the rest of the thermodynamic system.

The method developed by IEA/ECBCS Annex 42, in contrast to the above, is an intermediate level model that operates at the resolution of whole-building simulation. Such an approach accounts, on a time-step basis, for the interactions between the building and its environment, the occupants, the thermal and electrical production and distribution systems, and energy management and control systems. Furthermore, this model discretizes the SOFC-cogeneration system into groupings of components that comprise major sub-systems, such as those that produce electrical power, supply air, capture heat from the hot product gases, etc. In this manner, once the model is calibrated for a specific SOFC-cogeneration device analyses can be conducted to explore the benefits of improving the performance of individual sub-systems. For example, the impact of improving the heat recovery device upon overall system performance can be simulated without recalibrating the portions of the model that represent the fuel cell power module (FCPM), power conditioner, and other sub-systems. Additionally, such a structure facilitates the future development of more detailed modelling methods for specific sub-systems.

The model discretizes the SOFC-cogeneration system into nine control volumes:

1) The fuel cell power module which includes the stack, the afterburner, and the other components enclosed by the dashed line in Figure 1.
2) The air supply blower.
3) The fuel supply compressor.
4) The water pump.
5) An auxiliary burner.
6) An exhaust-gas-to-water heat exchanger.
7) A battery system for electrical storage.
8) A DC-AC power conditioning unit.
9) A dilution air system with optional heat recovery ventilator (not shown in Figure 1), as used in some systems to draw air through the cabinet to control skin losses to the containing room.

Each control volume is modelled in as rigorous a fashion as possible given the constraints of computational efficiency and the need to calibrate model inputs based upon the testing of coherent systems. (It is worth noting that the equations described in this section could

be recalculated over 100 000 times to perform a single annual simulation.)

The following sub-sections describe the methods used for resolving the exhaust-gas-to-water heat exchanger that is calibrated in section 6 using the directly measured and derived data described in sections 4 and 5. The interested reader is referred to an earlier paper (Beausoleil-Morrison, Schatz, and Maréchal, 2006) for a complete treatment of the model.

2.3 Exhaust Gas to Water Heat Exchanger (Sensible Heat Transfer)

A schematic representation of the control volume encapsulating the device that transfers heat from the auxiliary burner (or FCPM) control volume exhaust gases to the water loop connected to the building's HVAC system is shown in Figure 2. The state point labels shown in the figure are used in the development that follows.

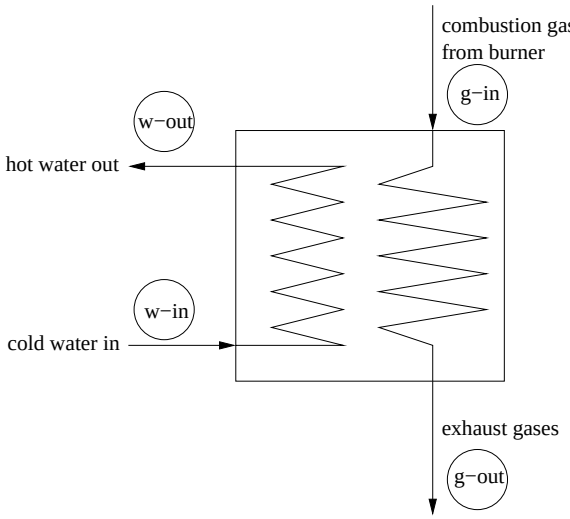

Figure 2: Heat exchanger control volume

The heat transfer from the hot gases to the water is characterized with the log mean temperature difference (LMTD) method for counterflow heat exchangers,

$$q_{HX} = (UA)_{eff} \cdot \frac{(T_{g-in} - T_{w-out}) - (T_{g-out} - T_{w-in})}{\ln\left(\frac{T_{g-in} - T_{w-out}}{T_{g-out} - T_{w-in}}\right)} \tag{1}$$

Where T_{g-in} is the temperature of the hot gases at the heat exchanger inlet, T_{g-out} is the temperature of the cooled gases that are exhausted to the ambient, T_{w-in} is the temperature of the cold water at the heat exchanger inlet, and T_{w-out} is the temperature of the warmed water exiting the heat exchanger. $(UA)_{eff}$ is the effective product of the heat transfer coefficient and area (W/K).

If it is assumed that heat loss from the heat exchanger to the ambient is negligible and that the heat capacity of each fluid stream remains constant through the heat exchanger, then the following energy balance can be written for the heat transfer between the fluid streams,

$$q_{HX} = (\dot{N}\hat{c}_P)_{g-in} \cdot (T_{g-in} - T_{g-out}) = (\dot{N}\hat{c}_P)_{w-in} \cdot (T_{w-out} - T_{w-in}) \quad (2)$$

Where $\hat{c}_P$ is the fluid's molar heat capacity (J/kmolK) and $\dot{N}$ is its molar flow rate (kmol/s). Subscript $g-in$ represents the state of the hot gas mixture as it enters the heat exchanger and subscript $w-in$ represents the state of the cold liquid water at the heat exchanger inlet.

Equation 2 can be rearranged to express the water outlet temperature as a function of the water inlet temperature and the gas temperatures,

$$T_{w-out} = T_{w-in} + \frac{(\dot{N}\hat{c}_P)_{g-in}}{(\dot{N}\hat{c}_P)_{w-in}} \cdot (T_{g-in} - T_{g-out}) \quad (3)$$

By substituting equation 3 into the numerator of equation 1 and by replacing q_{HX} with $(\dot{N}\hat{c}_P)_{g-in} \cdot (T_{g-in} - T_{g-out})$ from equation 2, it can be shown that,

$$\ln\left(\frac{T_{g-in} - T_{w-out}}{T_{g-out} - T_{w-in}}\right) = \frac{(UA)_{eff}}{(\dot{N}\hat{c}_P)_{g-in}} \cdot \left[1 - \frac{(\dot{N}\hat{c}_P)_{g-in}}{(\dot{N}\hat{c}_P)_{w-in}}\right] \quad (4)$$

By taking the exponential of each side of equation 4, substituting in equation 3, and rearranging, the gas outlet temperature can be expressed as a function of gas and water inlet temperatures,

$$T_{g-out} = \left\{ \frac{1 - \frac{(\dot{N}\hat{c}_P)_{g-in}}{(\dot{N}\hat{c}_P)_{w-in}}}{e^{\left[(UA)_{eff} \cdot \left(\frac{1}{(\dot{N}\hat{c}_P)_{g-in}} - \frac{1}{(\dot{N}\hat{c}_P)_{w-in}}\right)\right]} - \frac{(\dot{N}\hat{c}_P)_{g-in}}{(\dot{N}\hat{c}_P)_{w-in}}} \right\} \cdot T_{g-in} + \left\{ \frac{e^{\left[(UA)_{eff} \cdot \left(\frac{1}{(\dot{N}\hat{c}_P)_{g-in}} - \frac{1}{(\dot{N}\hat{c}_P)_{w-in}}\right)\right]} - 1}{e^{\left[(UA)_{eff} \cdot \left(\frac{1}{(\dot{N}\hat{c}_P)_{g-in}} - \frac{1}{(\dot{N}\hat{c}_P)_{w-in}}\right)\right]} - \frac{(\dot{N}\hat{c}_P)_{g-in}}{(\dot{N}\hat{c}_P)_{w-in}}} \right\} \cdot T_{w-in} \quad (5)$$

With the LMTD approach the effective product of the heat transfer coefficient and area must be evaluated at each time-step of the simulation. An approach is employed which casts $(UA)_{eff}$ as a parametric relation of the water and product gas flow rates (an alternate approach is available, as treated in Beausoleil-Morrison *et al.*, 2006),

$$(UA)_{eff} = hx_{s,0} + hx_{s,1} \cdot \dot{N}_w + hx_{s,2} \cdot \dot{N}_w^2 + hx_{s,3}\dot{N}_g + hx_{s,4} \cdot \dot{N}_g^2 \quad (6)$$

The form of equation 6 facilitates the determination of the $hx_{s,i}$ coefficients from experimental data, as will be shown in sections 3 through 6.

2.4 Exhaust Gas to Water Heat Exchanger (Latent Heat Transfer)

In the case of heat exchangers that are capable of condensing water from the exhaust gas stream, an additional term is added to equation 1 to account for the augmentation in heat

transfer due to condensation,

$$q_{HX} = q_{sensible} + q_{latent} \tag{7}$$

$$= (UA)_{eff} \cdot \frac{(T_{g-in} - T_{w-out}) - (T_{g-out} - T_{w-in})}{\ln\left(\frac{T_{g-in} - T_{w-out}}{T_{g-out} - T_{w-in}}\right)} + \dot{N}_{H_2O-cond} \cdot \hat{h}_{H_2O,fg}$$

Where $\dot{N}_{H_2O-cond}$ is the rate of condensation of water from the gas stream (kmol/s) and $\hat{h}_{H_2O,fg}$ is the molar heat of vapourization of water (J/kmol).

The sensible component of the heat exchange is determined as previously described (see equations 2 through 6). The rate of condensation is expressed in a parametric form that facilitates the determination of its coefficients from empirical data. The functional form of this parametric equation was established by recognizing that, for a given heat exchanger design, the rate of condensation will be primarily influenced by the concentration of water vapour in the gas stream and by the difference between the heat exchanger's temperature and the gas' dew point,

$$\dot{N}_{H_2O-cond} = (T_{cond-threshold} - T_{w-in}) \cdot \left[hx_{l,1} \cdot \left(\frac{\dot{N}_{H_2O}}{\dot{N}_{g-in}}\right) + hx_{l,2} \cdot \left(\frac{\dot{N}_{H_2O}}{\dot{N}_{g-in}}\right)^2 \right] \tag{8}$$

$\dot{N}_{H_2O}$ in equation 8 is the molar flow rate of water vapour in the gas stream entering the heat exchanger and $\dot{N}_{g-in}$ is the molar flow rate of all constituents of the gas.

$T_{cond-threshold}$ is a user-specified fixed value that represents the threshold of the water-inlet temperature above which condensation will not occur. When T_{w-in} is below $T_{cond-threshold}$ the condensation rate will be determined with equation 8. And when T_{w-in} is above $T_{cond-threshold}$ it is assumed that no condensation occurs. The model relies upon the user specifying $T_{cond-threshold}$ for the heat exchange device rather than attempting to calculate a dew point for the gas stream since this parameter is a function of heat exchanger design and gas pressure. Such a calculation would be complicated by the fact that the gas is pressurized (which affects the calculation of the dew point) and that it is unlikely that the user could specify sufficient data in order for the gas pressure to be calculated under various operating points.

Sections 3 through 6 discuss the methods used to determine the $hx_{l,i}$ coefficients and $T_{cond-threshold}$ for equation 8.

3. EXPERIMENTAL PROTOCOL

IEA/ECBCS Annex 42 has developed an experimental protocol (Beausoleil-Morrison and Kelly, 2005) that specifies the empirical data requirements for model calibration and validation. This document outlines the data that should be measured, the required measurement frequency, and the situations that should be assessed, and as such acts as a guide in experimental design.

For example, the required measurements include the following:

- Composition of fuel (molar fractions of CH_4, C_2H_6, N_2, etc.).

- Net AC electrical output from cogeneration device (after parasitic losses, battery losses , and losses from power conditioning unit).
- Gross DC power supplied by FCPM to power conditioning unit.
- Natural gas consumption rate (at standard temperature and pressure).
- Air supply rate (at standard temperature and pressure).
- Flow rate of exhaust gases through gas-to-water heat exchanger.
- Temperature of exhaust gases as they enter and exit the gas-to-water heat exchanger.
- Flow rate of water through gas-to-water heat exchanger.
- Temperature of water as it enters and exits the gas-to-water heat exchanger.

The protocol also recommends operating scenarios to examine. In one set of prescribed tests the cogeneration device is not operated as it would be in the field, but rather under controlled conditions which are designed to isolate the behaviour of a subset of the model's algorithms. Another set of tests reflects more realistic operation and is useful for verifying complete models and the interactions between algorithms within the models.

The first set of tests, which are ideally suited for model calibration, include the following:

- While the cogeneration device is operating with a constant electrical output, the temperature of the water supplied to the cogeneration device's heat exchanger is varied from 10°C to 90°C in approximately 5°C steps. Sufficient time is allowed for conditions to stabilize between each step change. The flow rate of the water through the heat exchanger remains constant at the recommended flow rate. The test is repeated at the minimum and maximum recommended flow rates.
- While the cogeneration device is operating with a constant electrical output, the flow rate of the water supplied to the cogeneration device's heat exchanger is varied from 50% of the recommended flow rate to 200% in approximately 10% steps. Sufficient time is allowed for conditions to stabilize between each step change. The temperature of the water supplied to the heat exchanger remains constant at 50°C. The test is repeated for a supply water temperature of 5°C and again for a supply water temperature of 80°C.
- If feasible, the above two test sequences are repeated at other constant electrical outputs. This will provide a "performance map" over the full range of cogeneration device outputs and thermal boundary conditions.
- The electrical load placed upon the cogeneration device is varied in a ramp over a given time period from no load to full load, subject to the restrictions of the experimental set-up and the operational requirements of the cogeneration device.

The above was used as a guide in designing a set of experiments that were performed with a a prototype 5 kW SOFC-cogeneration system developed by Fuel Cell Technologies[2]. The following section describes the experiments that were conducted.

[2] www.fct.ca

4. EXPERIMENTAL AND MEASUREMENT PROCEDURES

The experimental set-up that was configured to perform the tests outlined in the previous section is shown schematically in Figure 3. As that section elaborated, many of the tests required control over the water flow rate through the cogeneration device's heat exchanger and the water inlet temperature.

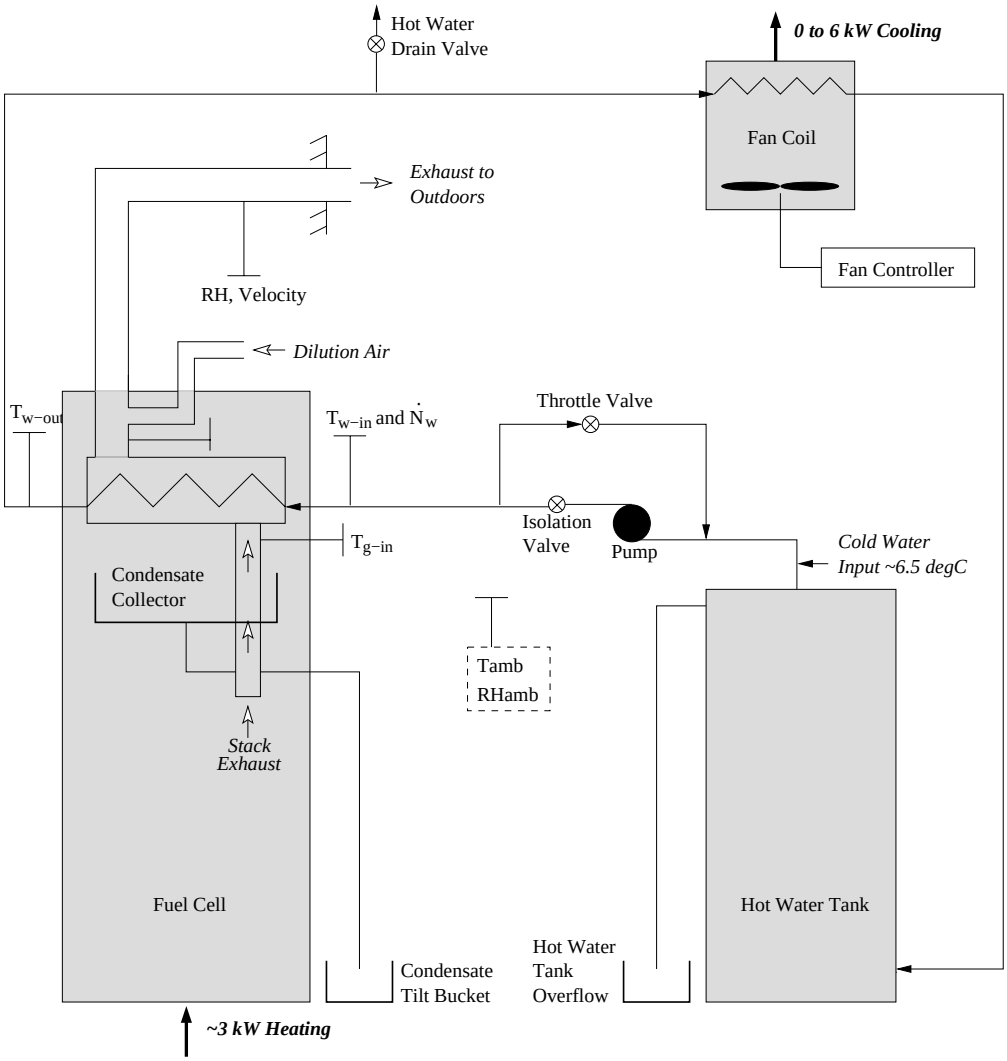

Figure 3: Experimental configuration to control flow rate and temperature of water entering the heat exchanger

Water was pumped from a storage tank to the cogeneration device's heat exchanger. From there the water flowed through a fan-coil before returning to the storage tank. As the circulating pump was operated at constant speed, the flow rate of water through the cogeneration device's heat exchanger was controlled by manually setting a throttling vale. An isolation valve downstream of the pump was manually controlled to increase back pressure, enabling a further reduction in the water flow rate through the heat exchanger. The lowest steady water flow rate through the heat exchanger that could be be achieved was 4 L/min. The highest flow rate was limited by the pump's capacity and was

approximately equal to 12 L/min.

The fan-coil was used to dissipate heat from the loop when the desired water temperature was greater than that of the room air. An on-off controller with a 0.2°C dead-band cycled the fan-coil on when necessary to achieve the desired water inlet temperature at the cogeneration device's heat exchanger. This resulted in a small degree of oscillation although the control was mostly satisfactory. When the desired water temperature was below that of the room air, warm water was drained downstream of the cogeneration device. This volume of water was replenished by adding cold water from the mains to the tank. The minimum heat exchanger water inlet temperature was thus regulated by the temperature of the water mains (approximately 6°C). The maximum temperature was restricted to 60°C in order to protect the circulating pump.

Once steady conditions were achieved, measurements were logged to file for a period of time to provide sufficient data to analyze the statistical variation of the measured and derived quantities for each test. Figure 4 illustrates the flow rate and heat exchanger water inlet temperature for the test that was configured to supply 30°C water to the heat exchanger at the lowest flow rate possible. As can be seen from the graph, ideal steady conditions could not be maintained over the duration of the test. Control over the water flow rate was found to be more stable than that over the water inlet temperature. In general, steady thermal conditions were more difficult to achieve at lower entering water temperatures. Notwithstanding, the variations in the water inlet temperature were deemed to be acceptable. The impact of these variations upon derived quantities will be illustrated in section 5.

The ramp tests described in section 3 required variation of the electrical output. This was achieved by varying the stack current demanded by the SOFC's internal controller.

The cogeneration device and the water loop were instrumented to record both electrical and thermal conditions throughout the tests. Voltage and current were measured at the points where power flowed to the power conditioning system, to the battery, and to the DC-powered ancillary devices. The AC output from the power conditioning system was also instrumented as were the AC-powered ancillary devices. Voltage taps were placed to measure DC voltage at the stack exit (i.e. at the start of the transmission cable carrying power to the PCU) and at the AC ancillary devices. A current shunt was installed to measure the total ancillary current draw. An watt transducer was used to monitor the AC output to the grid.

The flow rates of fuel supplied to the FCPM's stack and burner (fired to maintain stack temperatures when necessary) were measured independently using two mass flow controllers. Two venturi pressure transducers were used to measure the flow rates of air to the stack and burner.

The flow rate of water through the heat exchanger was measured at its inlet using a turbine water flow meter. Type-T thermocouples were used to measure the temperature of the water at the heat exchanger inlet and outlet. Gas temperatures were measured at the heat exchanger inlet and outlet using type-K thermocouples.

Due to the heat exchanger's design, when water vapour condensed from the exhaust gases the water droplets would drip onto the thermocouple measuring T_{g-in} (refer to Figure 2). This resulted in erroneous temperature readings, a fact that did not hinder model calibration efforts but rather assisted in identifying $T_{cond-threshold}$ in equation 8, as will be treated

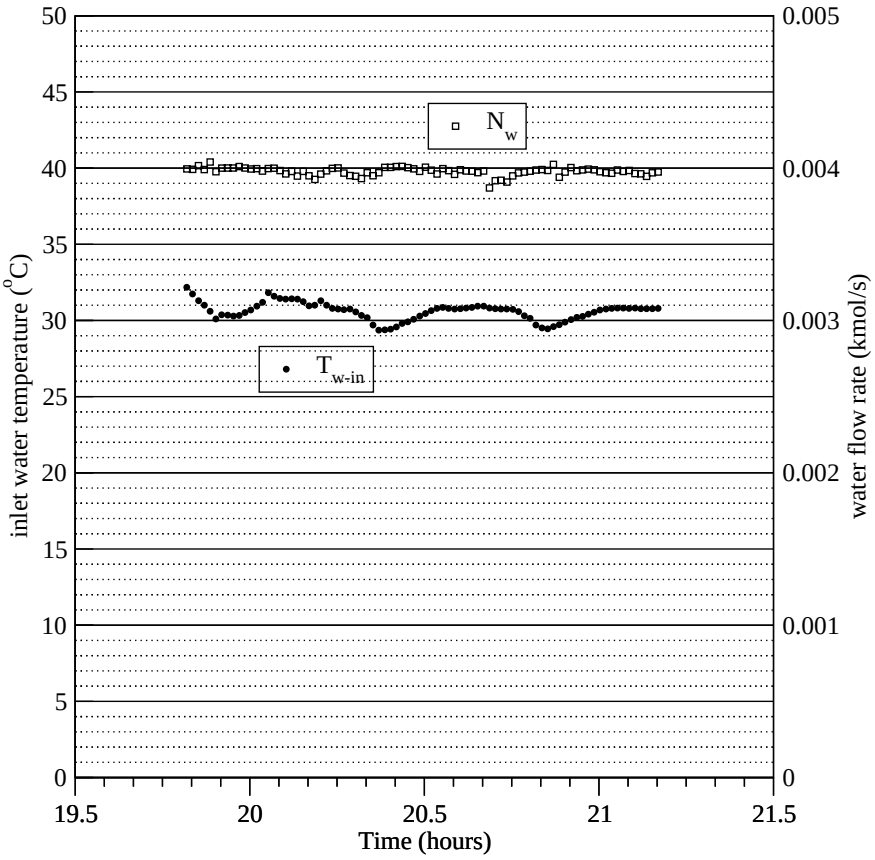

Figure 4: T_{w-in} and $\dot{N}_w$ over duration of one test

in section 6. The cogeneration device collects the condensate in an internal reservoir. When full, a float valve triggers a pump to drain this reservoir. A rain gauge tilt bucket was located to collect the pumped condensate to measure its volumetric flow rate. This gauge was calibrated to tilt for each accumulation of 8.24 mL.

The cogeneration device is designed such that the cooled gases exiting the heat exchanger are mixed with the dilution air that is drawn through the cabinet to control skin losses to the containing room. The temperature, velocity, and relative humidity of these mixed gases were measured downstream of the mixing point. A velocity probe was used to measure the velocity of this gas stream. Due to the configuration of the cogeneration device's exhaust chimney it was not possible to take these measurements in a region of fully developed flow. Rather, measurements had to be taken close to a 90° bend in the duct. During the exploratory phase of the work, the probe was inserted at numerous locations across the duct and the measured velocity profile examined to choose the most representative location to mount the probe. These limitations resulted in significant uncertainty in the measured flow rate of the combined gas stream.

Finally, the ambient temperature and relative humidity in the test room were measured approximately 1 m above the top of the fuel cell enclosure and approximately 1 m away from the air inlet side of the cogeneration device.

As detailed in the next section, the bias and precision errors from the primary measurements outlined above (e.g. temperatures, flow rates) propagate through into the derived quantities (e.g. $(UA)_{eff}$ of equation 1). In order to minimize the bias errors, a number of the instruments described above were calibrated. These include the water flow meter, the thermocouples at the heat exchanger's water inlet and outlet, the AC power flow meter, and the natural gas flow meter. These calibrations were effected by comparing instrument readings to reference instruments and then adjusting offset and slope parameters to adjust the translation of voltage signals to measured quantities.

Instantaneous measurements of the FCPM's DC power production, the FCPM's air and fuel supply rates, and the power flow to the battery were taken every second and the averages over the minute were logged to file. All other measurements were taken every 15 seconds and the four values averaged to log the data at each minute. The condensate flow rate was logged at the same frequency, but using a separate data acquisition system. Each of these measurements records the number of times the bucket had been tilted during the preceding minute. The time stamps in each file were used to synchronize the measurements.

Infrared images of the cogeneration device were captured during one test at which the cogeneration device was producing its maximum power. Three of the four side faces and the top of the SOFC enclosure provided unobstructed views for the imaging. These images were used to derive thermal contour maps by taking into account the surface emissivities.

A gas chromatograph was used to analyze the content of natural gas supply a few days prior to the experiments. This determined the molar fractions of each constituent of the gas supply in order to accurately determine its lower heating value.

5. CALCULATION OF CALIBRATION DATA AND ANALYSIS OF UNCERTAINTIES

The previous section detailed the measurement taken during the experiments. In order to calibrate and validate the model, these primary measurements were used to derive the variables of interest to the model. This section details the calculation of these derived quantities and their associated uncertainties. The methods illustrated here for treating the exhaust-gas-to-water heat exchanger equally apply to other quantities, such as the electrical efficiency of the FCPM, the DC-AC conversion efficiency of the power conditioning system, etc.

As discussed in section 2.3, the equation relating the effective product of the heat transfer coefficient and area to the flow rates of water and gas through the heat exchanger (refer to equation 6) must be calibrated from the experimental data. Referring to equations 1 and 2, it can be shown that $(UA)_{eff}$ can be derived from five of the primary measurements described in section 4,

$$(UA)_{eff} = \frac{(\dot{N}\hat{c}_P)_{w-in} \cdot (T_{w-out} - T_{w-in})}{\left[\frac{(T_{g-in} - T_{w-out}) - (T_{g-out} - T_{w-in})}{\ln\left(\frac{T_{g-in} - T_{w-out}}{T_{g-out} - T_{w-in}} \right)} \right]} \tag{9}$$

Equation 9 was evaluated for each minute of recorded data using the four temperature readings (T_{w-in}, T_{w-out}, T_{g-in}, T_{g-out}) and the water flow rate measurement ($\dot{N}_{w-in}$). The heat capacity of the water entering the heat exchanger ($\hat{c}_{P,w-in}$) was calculated from T_{w-in} using a parametric relation (Beausoleil-Morrison, Schatz, and Maréchal, 2006).

The method recommended by the American Society of Mechanical Engineers (described in Abernethy *et al.*, 1985 and Moffat, 1988) was used to calculate the uncertainties of the measured quantities and to propagate these uncertainties into the derived quantities. With this a bias error was assigned to each primary measurement. These were established based upon the instrumentation specifications, either an absolute error as a percent of full-scale measurement and/or a reading error as a percent of the value measured. Where instruments were calibrated (refer to section 4) the bias error was established based upon the calibration parameters. In these cases, the bias error was set based upon either the average or maximum deviation of the corrected measured values to the reference values.

In some cases additional bias errors were assigned based upon judgement. For example, a substantial bias error was assigned to the velocity measurement of the combined exhaust gas stream due to the restrictions on instrument placement, as discussed in section 4. As another example, an additional bias error was assigned the condensate flow rate measurement. As described in section 4, condensate is measured by a rain gauge tilt bucket after it is pumped from an internal reservoir. The time lag between the pumping and measurement actions introduced some uncertainly to the condensate flow rate measurement. Consequently a bias error of 50 mL (the approximate volume of the internal reservoir) was assigned to the measurement of the condensate flow over the duration of each experiment.

The total bias for each measurement point is calculated from the individual bias errors for that sensor using the root-sum-square method,

$$B = \left[B_1^2 + B_2^2 + \cdots + B_k^2 \right]^{1/2} \tag{10}$$

For each of the tests specified in section 3 the desired boundary conditions (e.g. T_{w-in} and $\dot{N}_{w-in}$) were held for a period of time and data logged each minute. The precision index of a single measurement within a given test is calculated based on the average value of the observed parameter during that test and the number of logged readings,

$$S = \left[\frac{\sum_{i=1}^{N} \left(X_i - \bar{X} \right)^2}{N-1} \right]^{1/2} \tag{11}$$

Where N is the number of logged readings. It is worth noting that the data were logged at one-minute intervals based upon either one second or 15 second instantaneous readings (refer to section 4). The X_i values of equation 11 are the one-minute averaged values since the instantaneous data were not logged. It is also worth noting that S has the same value for each data point within a given test.

The precision index of the average value of a parameter for a given test is lower than that for the individual measurements according to,

$$S_{avg} = \frac{S}{\sqrt{N}} \tag{12}$$

Finally, the bias and precision indices are combined to express the uncertainty in a measured quantity,

$$U_{95\%} = \sqrt{B^2 + (t \cdot S)^2} \tag{13}$$

$$U_{99\%} = B + t \cdot S \tag{14}$$

Where $U_{95\%}$ and $U_{99\%}$ are the measurement uncertainties at the 95 and 99 percent confidence levels, respectively. t is the standard statistical Student t value and is a function of the value of N used in evaluating equation 11.

The uncertainty of a derived quantity is determined by propagating the bias and precision indices of the measurements that are used to calculate the derived quantity. For example, the bias error for $(UA)_{eff}$ is calculated as follows (refer to equation 9),

$$B_{(UA)_{eff}} = \left[\left(\frac{\partial (UA)_{eff}}{\partial \dot{N}_{w-in}} \cdot B_{\dot{N}_{w-in}} \right)^2 + \left(\frac{\partial (UA)_{eff}}{\partial T_{w-out}} \cdot B_{T_{w-out}} \right)^2 + \left(\frac{\partial (UA)_{eff}}{\partial T_{w-in}} \cdot B_{T_{w-in}} \right)^2 \right. \tag{15}$$

$$\left. + \left(\frac{\partial (UA)_{eff}}{\partial T_{g-in}} \cdot B_{T_{g-in}} \right)^2 + \left(\frac{\partial (UA)_{eff}}{\partial T_{g-out}} \cdot B_{T_{g-out}} \right)^2 \right]^{1/2}$$

The precision index for $(UA)_{eff}$ is determined in a similar manner and the overall uncertainty determined using equations 13 and 14.

The propagation of measurement uncertainties into equation 15 is demonstrated by examining the test that was illustrated in Figure 4. The bias errors and precision indices for the four temperature and one water flow rate measurements used in the equation are summarized in Table 1. The bias errors reported in the table are the average for the 82 measurement points of the test. Likewise, the precision index is that corresponding to each individual measurement, and not the precision index of the set average (i.e. it represents S of equation 11, not S_{avg} of equation 12).

Table 1: Uncertainty parameters for test at $T_{w-in} = 30^o C$ and $\dot{N}_w = 0.004 kmol/s$

measurement	**average value over test**	**B**	**S**	$U_{95\%}$
T_{w-in}	30.60°C	0.10°C	0.58°C	1.17°C
T_{w-out}	43.38°C	0.10°C	0.48°C	0.97°C
T_{g-in}	284.27°C	2.20°C	0.57°C	2.48°C
T_{g-out}	45.04°C	2.20°C	0.36°C	2.32°C
$\dot{N}_w$	$4.0 \cdot 10^{-3} kmol/s$	$7.9 \cdot 10^{-5} kmol/s$	$2.7 \cdot 10^{-5} kmol/s$	$9.3 \cdot 10^{-5} kmol/s$

Table 1 also lists the average uncertainty at the 95% confidence level of the 82 measurements of each of the five parameters. As can be seen, the precision indices are the predominant determinant of the uncertainty of the water temperature measurements, an observation consistent with the T_{w-in} measurements plotted in Figure 4. In contrast, the instrument bias errors are the predominant determinants of the uncertainty of the gas temperatures and the water flow rate.

Equation 9 was applied to calculate the $(UA)_{eff}$ value for each of the 82 measurement points of the test. The procedure outlined in equations 10, 11, 13, and 15 was then applied to calculate the uncertainty for each of these 82 derived $(UA)_{eff}$ values. Figure 5 plots these derived values and their uncertainties. The test-averaged $(UA)_{eff}$ value determined from the 82 measurement points and its error bar are also shown in the figure. The uncertainty of the test-averaged $(UA)_{eff}$ value is less than that for individual measurements due to equation 12.

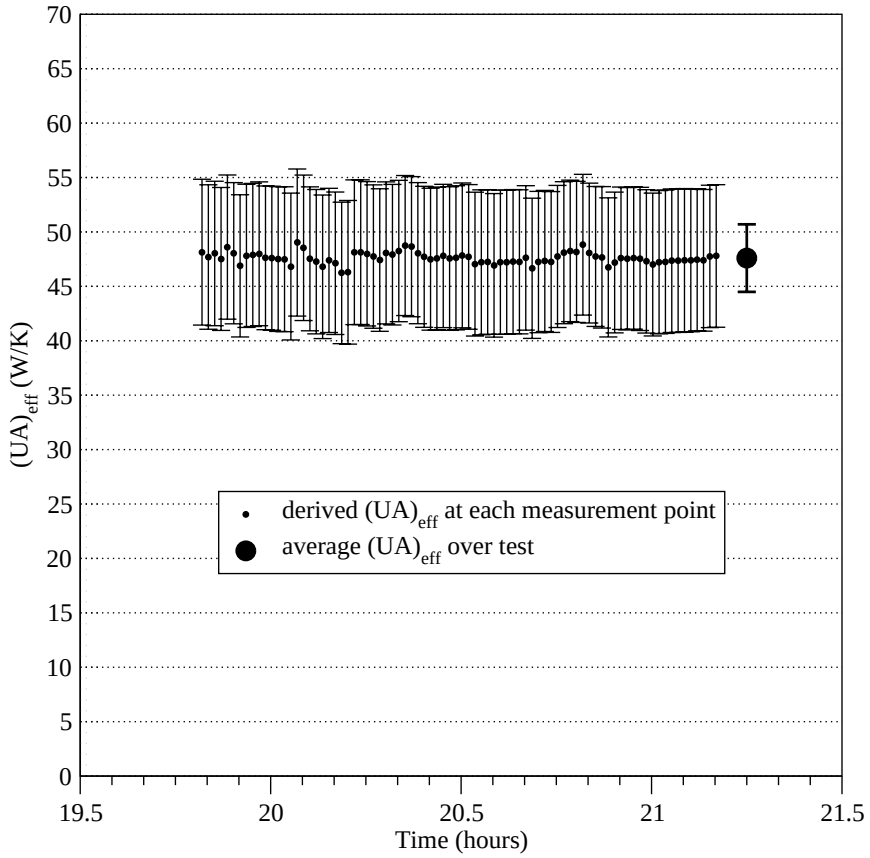

Figure 5: Derived $(UA)_{eff}$ values and associated 95% error bars for $T_{w-in} = 30^{o}C$ and $\dot{N}_w = 0.004 kmol/s$

The procedure outlined in this section was applied to each test to produce a set of 17 test-averaged $(UA)_{eff}$ values at various combinations of T_{w-in}, N_w, and N_g. This set of data represent the calibration data set, the subject of the next section.

6. MODEL CALIBRATION

The calibration tests described in the previous sections yielded 17 derived values of $(UA)_{eff}$ at various water ($\dot{N}_w$) and gas ($\dot{N}_g$) flow rates. This section discusses how the data from these 17 tests were used to calibrate the heat exchanger's sensible heat transfer characteristics. The calibration of the heat exchanger's latent heat transfer characteristics using data from other tests is also treated.

A non-linear regression method was used to establish the values of the $hx_{s,i}$ coefficients that produced the best fit to equation 6. The values of the coefficients determined from this analysis are presented in Table 2.

Table 2: Calibrated coefficients for equation 6

$hx_{s,0}$	83.1
$hx_{s,1}$	4 798
$hx_{s,2}$	$-138 \cdot 10^3$
$hx_{s,3}$	$-353.8 \cdot 10^3$
$hx_{s,4}$	$5.15 \cdot 10^8$

Figure 6 compares the $(UA)_{eff}$ determined with equation 6 and the coefficients of Table 2 with the $(UA)_{eff}$ values derived from the measurements. The uncertainty bars determined in section 5 are plotted in the figure. The left side of the figure provides a view normal to the $\dot{N}_g$ axis while the right side provides a view normal to the $\dot{N}_w$ axis. As can be seen, the functional form of equation 6 well represents the dependency of $(UA)_{eff}$ on the two flow rates. The calibrated values lie within the error bars for each of the 17 data points.

Figure 7 provides another indication of the goodness of fit between the calibrated $(UA)_{eff}$ values and those derived from measurements. The coefficient of determination (r^2 value) was 0.98. The average error (difference between the calibrated $(UA)_{eff}$ value and that derived from measurements) was 1.9% while the room-mean-square error was 2.1%. The maximum error for a single point was 3.2%.

A number of tests, in addition to the 17 described above, were conducted to explore the operation of the heat exchanger under condensing conditions. One of these tests was configured to identify $T_{cond-threshold}$ of equation 8. This variable represents the threshold of the water inlet temperature above which condensation does not occur. The examination of the tilt bucket readings during preliminary testing indicated an approximate range within which $T_{cond-threshold}$ lay. However, each of these tests was time consuming. As elaborated in section 4, the tilt bucket instrument was filled only after the cogeneration device's internal condensate reservoir became filled and was pumped out. Steady conditions had to be held for long periods of time (in some cases many hours) in order to register readings at the tilt bucket.

Section 4 explained how the formation of condensation from the exhaust gases led to erroneous T_{g-in} thermocouple readings. Advantage was taken of this fact to calibrate $T_{cond-threshold}$ for equation 8. By controlling the water loop illustrated in Figure 3, T_{w-in} was slowly reduced from 33°C, which the preliminary testing had indicated was above $T_{cond-threshold}$. For the FCPM's electrical output exercised in this test, T_{g-in} was

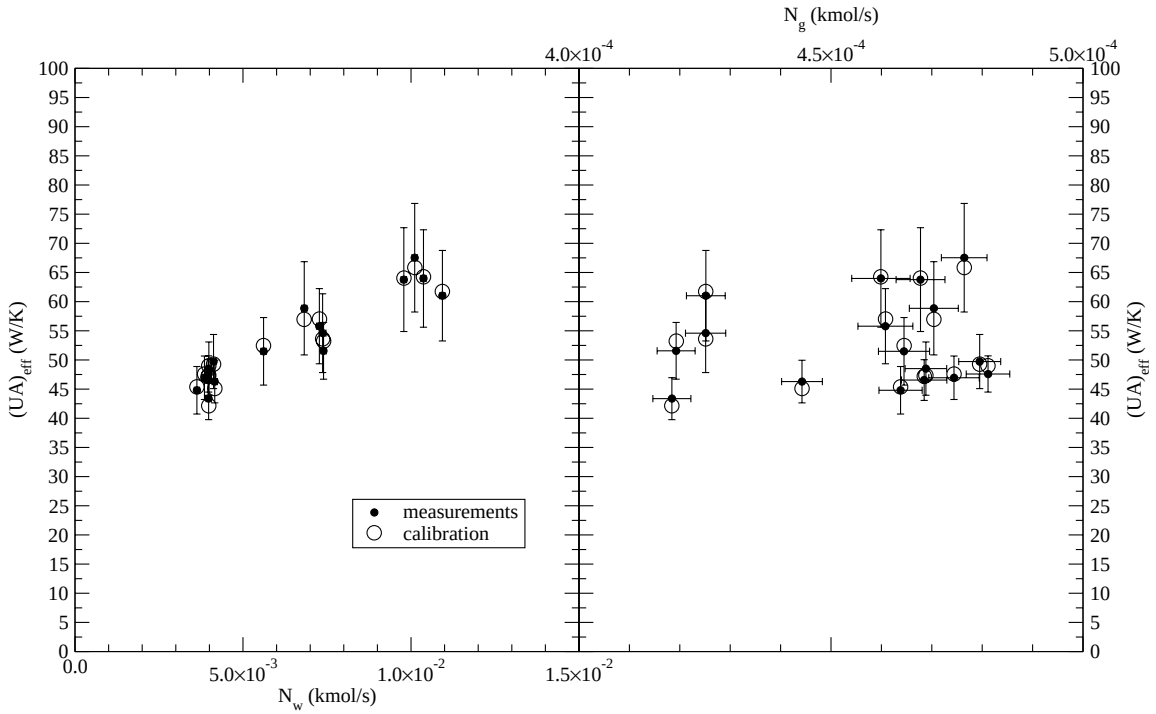

Figure 6: Calibrated $(UA)_{eff}$ versus measurements as a function of $\dot{N}_w$ (left) and $\dot{N}_g$ (right)

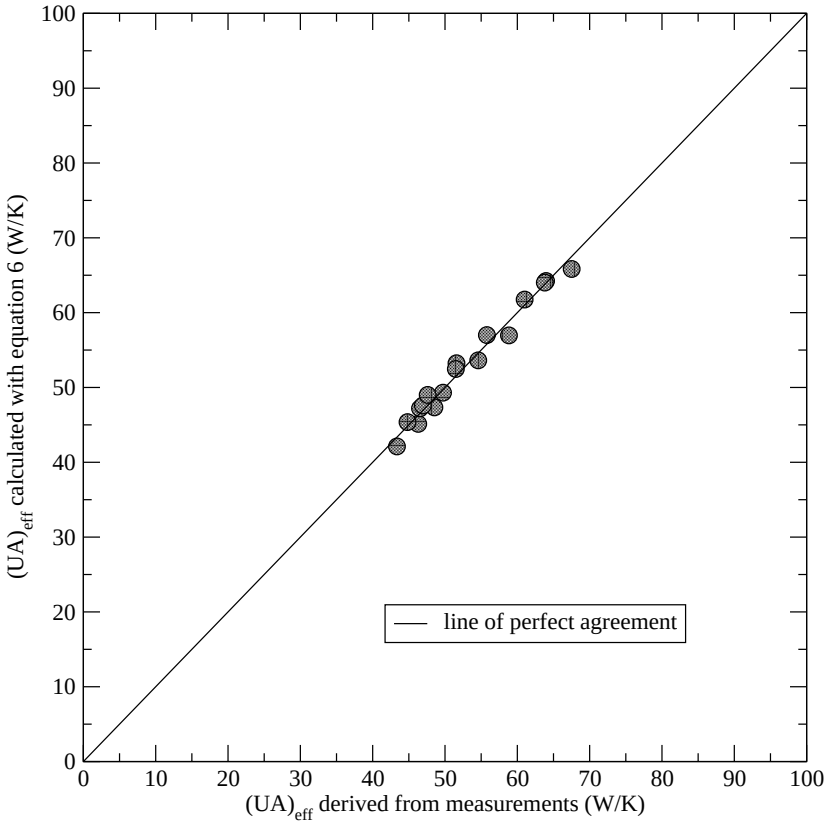

Figure 7: Goodness of fit between calibrated and measured $(UA)_{eff}$

approximately 280°C. As shown in Figure 8 the thermocouple produced reliable data for the first portion of the test. The thermocouple, however, began producing unreliable readings once T_{w-in} was reduced to 23°C. This event indicated the first formation of liquid water which dripped onto the thermocouple. Even as the inlet water temperature was warmed to 35°C, the thermocouple continued to produce unreliable readings, indicating that condensation continued to form. It took considerable time for the thermocouple readings to stabilize. This tends to indicate that although the onset of condensation requires a low value of T_{w-in}, once condensing conditions have been achieved condensation can occur at warmer temperatures. Based upon this test it was decided to set $T_{cond-threshold}$ to 35°C.

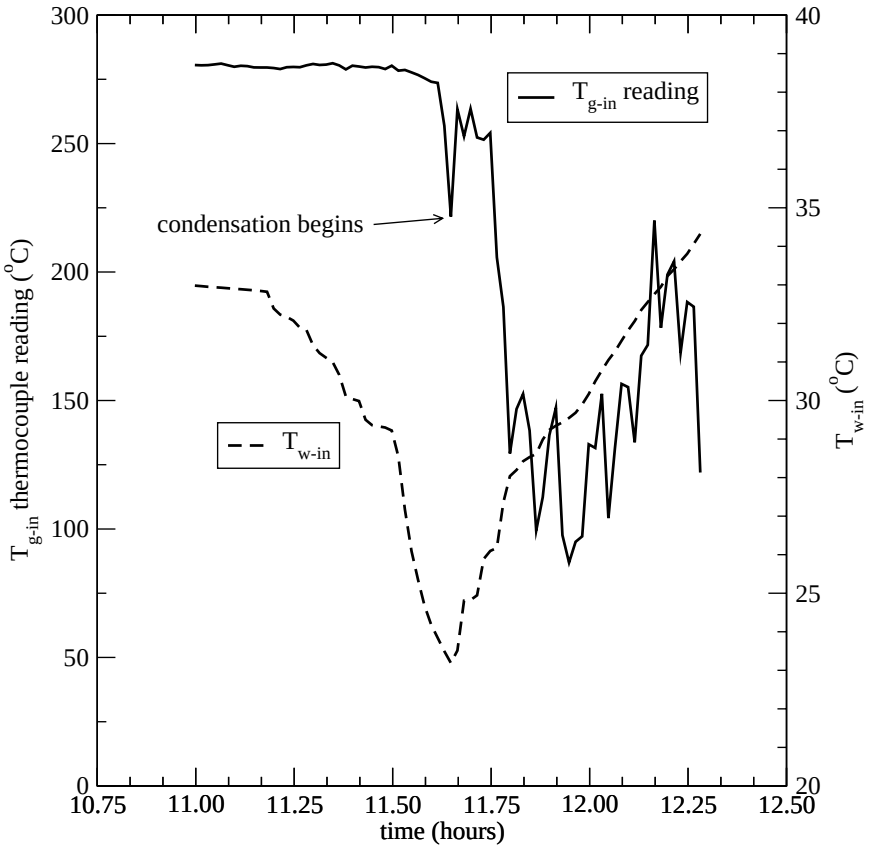

Figure 8: Identification of $T_{cond-threshold}$

A series of 7 tests were then conducted at various water flow rates and values of T_{w-in} in order to establish the $hx_{l,i}$ coefficients of equation 8. Sufficient time was allowed in each test to achieve steady conditions. Due to practical constraints, however, these tests could only be conducted with a nearly constant ratio of water vapour in the exhaust gas stream (refer to $\dot{N}_{H_2O}/\dot{N}_{g-in}$ in equation 8). (This is determined by the FCPM's operating point.)

A non-linear regression method was used to establish the values of the $hx_{l,i}$ coefficients that produced the best fit to equation 8. As elaborated above, $T_{cond-threshold}$ was set to 35°C to perform this regression. The values of the coefficients determined from this analysis are presented in Table 3.

Table 3: Calibrated coefficients for equation 8

$hx_{l,1}$	$-1.96 \cdot 10^{-4}$
$hx_{l,2}$	$3.1 \cdot 10^{-3}$

Figure 9 compares the $\dot{N}_{H_2O-cond}$ determined with equation 8 and the coefficients of Table 3 with the $\dot{N}_{H_2O-cond}$ values derived from the measurements. The coefficient of determination (r^2 value) was 0.96. The average error (difference between calibrated values and those derived from measurements) was $10^{-6} kmol/s$[3] while the room-mean-square error was $1.2 \cdot 10^{-6} kmol/s$. The maximum error for a single point was $2.1 \cdot 10^{-6} kmol/s$. The uncertainty bars determined in section 5 are plotted in the figure. As can be seen, the functional form of equation 7 reasonably represents the dependency of $\dot{N}_{H_2O-cond}$ upon T_{w-in}. The calibrated values lie within the error bars for five of the seven data points. The greatest deviation between measurement and calibration occurs at $T_{w-in} \approx 30^o C$ where the condensation flow rate is very small.

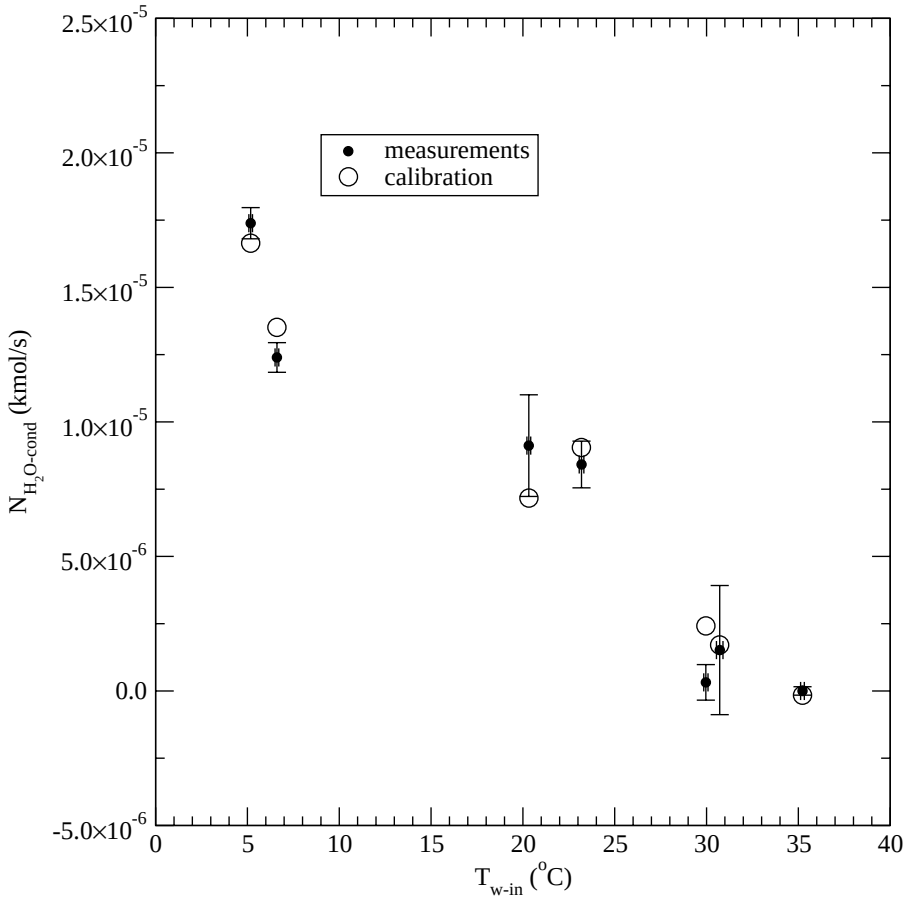

Figure 9: Goodness of fit between calibrated and measured $\dot{N}_{H_2O-cond}$

[3] To place these numbers in context, a condensation rate of $10^{-6} kmol/s$ results in approximately 40 W of heat transfer.

It is important to note that the correlation coefficients presented in Tables 2 and 3 are only valid within the range of water and flow rates examined. In particular these experiments examined only a narrow range of gas flow rates and the ratio of water vapour in the exhaust gas stream ($\dot{N}_{H_2O}/\dot{N}_{g-in}$) was nearly constant throughout the tests.

7. CONCLUSIONS AND RECOMMENDATIONS FOR FUTURE WORK

This paper has demonstrated the methods that are being used to calibrate a model that has been developed by IEA/ECBCS Annex 42 for simulating the thermal and electrical production of SOFC-cogeneration devices within whole-building simulation programs. The experimental procedures that were employed to test a prototype 5 kW SOFC-cogeneration system were described in detail. The experimental configuration, types of instrumentation employed, and the operating scenarios examined were treated. The propagation of measurement uncertainty into the derived quantities that are necessary for model calibration was demonstrated by focusing upon the SOFC-cogeneration system's gas-to-water heat exchanger. The techniques employed to then calibrate the pertinent aspects of the model using these measured data were then demonstrated.

This paper presented the results of the calibration of the sensible heat transfer characteristics of the heat exchanger. This calibration was conducted using measured data derived from 17 tests which spanned a range of water flow rates and entering water temperatures. Likewise, the calibration of the latent heat transfer characteristics was conducted with measured data from 8 tests (one to establish the threshold of the water-inlet temperature above which condensation will not occur and the other 7 to regress coefficients). The goodness of fit of these correlations was demonstrated by comparison with the measured data from which they were derived. This demonstrates that the correlations well represent the measured data. However, it does not speak to the validity of the calibrated model for representing other conditions. Additional tests were conducted on the prototype SOFC-cogeneration device. In the future, simulations with the calibrated model will be compared to these additional data. This will represent a more rigorous test of the quality or validity of the calibration presented here.

The reader is cautioned that the calibrated inputs presented in this paper are only valid within the ranges of independent variables examined in the experiments. In particular these experiments examined only a narrow range of gas flow rates and the ratio of water vapour in the exhaust gas stream was nearly constant throughout the tests. It is hoped that further experimental work planned by other IEA/ECBCS Annex 42 partners will be able to examine additional operating points to extend the validity of the calibrated model.

The methods elaborated here for calibrating the heat exchanger will be applied to all other aspects of the IEA/ECBCS Annex 42 SOFC-cogeneration model, including the FCPM electrical efficiency, air supply rate, thermal losses from the skin, power conditioning efficiency, etc. The results of these efforts will be reported in future papers. Future papers will also report the results of simulations conducted with the fully calibrated model to assess the performance of SOFC-cogeneration devices under different operating scenarios and coupled to houses with various thermal and electrical demand characteristics.

ACKNOWLEDGEMENTS

The work described in this paper was undertaken as part of the International Energy Agency's Energy Conservation in Building and Community Systems Programme's Annex 42 *The Simulation of Building-Integrated Fuel Cell and Other Cogeneration Systems* (www.cogen-sim.net). The Annex is an international collaborative research effort and the authors gratefully acknowledge the indirect or direct contributions of the other Annex participants.

REFERENCES

Abernethy, R.B., Benedict, R.P., and Dowdell, R.B., "ASME Measurement Uncertainty," *Journal of Fluids Engineering*, 107, pp. 161-164 (1985).

Beale, S.B., Lin, Y., Zhubrin, S.V., and Dong, W., "Computer Methods for Performance Prediction in Fuel Cells," *Journal of Power Sources*, 118, pp. 79-85 (2003).

Beausoleil-Morrison, I. and Kelly, N., "Protocol for Conducting Experiments on Cogeneration Devices," *IEA/ECBCS Annex 42 Working Document* (2005).

Beausoleil-Morrison, I., Schatz, A., and Maréchal, F., "A Model for Simulating the Thermal and Electrical Production of Small-Scale Solid-Oxide Fuel Cell Cogeneration Systems within Building Simulation Programs," *HVAC&R Research Special Issue*, 12, 3a, pp. 641-667 (2006).

Bove, R., Lunghi, P., and Sammes, N.M., "SOFC Mathematical Model for Systems Simulations. Part 1: From a Micro-Detailed to Macro-Black-Box Model," *Int Journal of Hydrogen Energy*, 30, pp. 181-187 (2005).

Braun, R.J., *Optimal Design and Operation of Solid Oxide Fuel Cell Systems for Small-Scale Stationary Applications, Ph.D. Thesis*, University of Wisconsin-Madison, USA (2002).

Dorer, V., Weber, R., and Weber, A., "Performance Assessment of Fuel Cell Micro-Cogeneration Systems for Residential Buildings," *Energy and Buildings*, 37, pp. 1132-1146 (2005).

Ellis, M.W. and Gunes, M.B., "Status of Fuel Cell Systems for Combined Heat and Power Applications in Buildings," *ASHRAE Transactions*, 108, 11, pp. 1032-1044 (2002).

Hawkes, A. and Leach, M., "Solid Oxide Fuel Cell Systems for Residential Micro-Combined Heat and Power in the UK: Key Economic Drivers," *Journal of Power Sources*, 149, pp. 72-83 (2005).

Knight, I. and Ugursal, V.I., "Residential Cogeneration Systems: A Review of the Current Technologies," *IEA/ECBCS Annex 42 Report* (2005).

Moffat, R.J., "Describing the Uncertainties in Experimental Results," *Experimental Thermal and Fluid Science*, 1, pp. 3-17 (1988).

Sicre, B., Bühring, A., and Platzer, B., "Energy and Financial Performance of Micro-CHP in Connection with High-Performance Buildings," *Proc. Building Simulation 2005*, pp. 1139-1146, Montréal Canada (2005).

Singhal, S.C. and Kendall K., *High Temperature Solid Oxide Fuel Cells: Fundamentals, Design, and Applications,* Elsevier, Oxford UK (2003).